Modeling the solid-to-plasma transition for laser imprinting in direct-drive inertial confinement fusion

G. Duchateau,[1,*] S. X. Hu,[2] A. Pineau,[1] A. Kar,[2] B. Chimier,[1] A. Casner,[1] V. Tikhonchuk,[1,3] V. N. Goncharov,[2]
P. B. Radha,[2] and E. M. Campbell[2]

[1]*Université de Bordeaux-CNRS-CEA, Centre Lasers Intenses et Applications, UMR 5107, 351 Cours de la Libération, 33405 Talence Cedex, France*
[2]*Laboratory for Laser Energetics, University of Rochester, 250 E. River Rd, Rochester, New York, USA*
[3]*ELI-Beamlines, Institute of Physics, Czech Academy of Sciences, Za Radnicic 835, 25241 Dolni Bgezany, Czech Republic*

(Received 10 April 2019; revised manuscript received 4 July 2019; published 3 September 2019)

Laser imprinting possesses a potential danger for low-adiabat and high-convergence implosions in direct-drive inertial confinement fusion (ICF). Within certain direct-drive ICF schemes, a laser picket (prepulse) is used to condition the target to increase the interaction efficiency with the main pulse. Whereas initially the target is in a solid state (of ablators such as polystyrene) with specific electronic and optical properties, the current state-of-the-art hydrocodes assume an initial plasma state, which ignores the detailed plasma formation process. To overcome this strong assumption, a model describing the solid-to-plasma transition, eventually aiming at being implemented in hydrocodes, is developed. It describes the evolution of main physical quantities of interest, including the free electron density, collision frequency, absorbed laser energy, temperatures, and pressure, during the first stage of the laser-matter interaction. The results show that a time about 100 ps is required for the matter to undergo the phase transition, the initial solid state thus having a notable impact on the subsequent plasma dynamics. The nonlinear absorption processes (associated to the solid state) are also shown to have an influence on the thermodynamic quantities after the phase transition, leading to target deformations depending on the initial solid state. The negative consequences for the ICF schemes consist in shearing of the ablator and possibly preliminary heating of the deuterium-tritium fuel.

DOI: 10.1103/PhysRevE.100.033201

I. INTRODUCTION

Inertial confinement fusion (ICF) has been actively pursued over the past four decades in laboratories [1–6]. In the direct-drive ICF scheme [4–6], many intense laser beams are focused on a spherical capsule surface to ablate target material, thereby driving the deuterium-tritium-contained capsule to implode through the so-called "rocket effect." The overlapped laser beams consisting of many speckles can give a certain amount of intensity nonuniformity on the ICF target surface. Consequently, such spatial variations of laser intensity can cause nonuniform ablation on the ICF target surface, leading to a rough ablation surface and nonuniform shocks. This so-called laser-imprinting process [7] has been a concern since the beginning of direct-drive ICF because the laser-imprint-induced ablation surface modulation can be exponentially amplified by Rayleigh-Taylor (RT) instability during the target acceleration phase. If not properly controlled, the laser-imprint-induced RT instability can detrimentally degrade ICF target performance. Both experimental and simulation evidence [8–11] has indicated that laser imprinting is the major cause for degrading implosion performance of low-adiabat ($\alpha = 2 - 3.5$) and high-convergence ($C_R > 22$) targets, where the adiabat α is conventionally defined as the ratio of deuterium-tritium (DT)-shell pressure to its Fermi-degenerate pressure, i.e., $\alpha = P/P_F$; while the convergence ratio is defined as the ratio of initial target radius to the final hot-spot radius, i.e., $C_R = R_0/R_{\text{hot-spot}}$. Thus, understanding and mitigating laser-imprint effects are essential to the success of direct-drive ICF.

Understanding the laser-imprint effects on direct-drive ICF implosions relies on radiation-hydrodynamics simulations. However, the detailed process of the laser-induced solid-to-plasma transition is currently missing in ICF hydrocodes. Instead, the current hydrocodes assume that the ICF target ablator is already in the plasma state at the very beginning ($t = 0$), i.e., having a free-electron density n_e larger than the critical electron density (n_c) of the drive laser. For the commonly used hydrocarbon polymer ablators such as polystyrene (CH) and glow discharge polymer, this assumption of $n_e > n_c$ at $t = 0$ is obviously invalid since these dielectric materials have no free (conduction) electrons at all before laser irradiation. How laser speckles create free electrons to form plasmas should affect the laser imprinting process. For example, under the current wrong assumption of a plasma state at $t = 0$, the laser-induced shock pressure modulation $\delta P/P$ is linearly proportional to the laser intensity modulation $\delta I/I$. However, once the realistic multiphoton-tunneling ionization and impact ionization processes are correctly considered for the initial solid-to-plasma transition, the target is expected to have a nonlinear response to the spatial laser-intensity modulation. This has been evidenced by recent two-dimensional VISAR measurements of spatial modulation in shock velocity, which showed a significant discrepancy between the current

---

[*] guillaume.duchateau@u-bordeaux.fr

hydrosimulation and experiment [12]. Moreover, in contrast to an initial plasma state (currently used in hydrocodes), a dielectric material is initially transparent for the commonly used drive laser at a wavelength $\lambda = 351$ nm. So laser energy could be deposited far from the target surface, with a spatial profile along the laser propagation direction. This is drastically different from the current treatment of assuming an initial plasma state in which the laser energy deposition is limited only to the over-critical target surface. In this approach, the penetration of initial part of laser pulse inside the target is ignored. This so-called "shine-through" effect [13] may produce undesirable preheating of the ablator and fuel. Therefore, there is a need to develop a physics-based model to better capture the initial plasma formation process for direct-drive ICF simulations of laser imprinting.

This paper is devoted to developing such a model for better describing the initial laser-target interaction during the transition from the initial solid state to the plasma state (critical electron density formed) and the evolution of thermodynamic quantities such as the electron and ion-lattice (lattice of neutral atoms early in the interaction, going to a lattice of ions after ionization) temperature and pressure. It is first based on a microscopic description of the electron dynamics within a simplified band structure relevant to dielectric materials, allowing us to describe the evolution of the produced free electron density with respect to time and space. Photoionization, impact ionization, and electron recombination are described. A Drude model then allows us to evaluate the absorbed laser energy [14,15]. The involved electron collision frequency depends on the state of matter, accounting initially for only collisions with phonons, and finally collisions with ions in the plasma state. This absorbed laser energy is introduced as a source term in a two-temperature model to evaluate both electron and ion-lattice temperatures. Finally, the previous description is coupled to a Beer-Lambert law to describe the laser intensity depletion inside the target. Numerical simulations have been performed with laser parameters relevant to the direct-drive ICF scheme. Despite some modeling approximations, this approach provides useful trends and conclusions within the present context. The results show clearly the influence of the initial solid state and laser intensity distribution on the macroscopic structure of the ablator and fuel.

In what follows we consider the interaction of a laser with a standard direct drive ICF target [5] containing a 8 μm thick ablator and 50 μm and 400 μm thick solid and gas DT mixture, respectively. Namely, we estimate the spatial profile of absorbed energy along the laser propagation axis, in comparison with the current treatment, in order to highlight the interest of modeling the solid-to-plasma transition. We in particular focus on the amount of energy absorbed in the ablator bulk before entering the plasma state because it may affect the shock timing and the fuel adiabat during the implosion. Eventually, our laser-imprinting model will be implemented into radiation-hydrodynamics codes for direct-drive ICF simulations.

The paper is organized as follows. Section II introduces the solid-to-plasma transition modeling for the laser energy absorption. All main ingredients described previously are detailed. Modeling results and discussions are presented in Sec. III. The temporal evolutions of the free electron density and temperatures are first provided to exhibit the main mechanisms at play and demonstrate the reliability of the proposed model. Laser propagation across the ablator and energy deposition are then considered. In Sec. IV, by evaluating the induced pressure, we are allowed to evaluate the mechanical deformations of the ablator and stresses at the ablator-fuel interface, exhibiting the possible consequences of the initial solid state on the generation of spatial nonuniformities. Possible consequences of considering an initial solid state (not plasma) on the DT fuel are finally provided. Conclusions and outlooks are drawn in Sec. V.

II. MODELING

We consider here the early interaction of the laser picket with intensities about 10^{13}–10^{14} W/cm^2 with an initially cold target on a timescale of 100 ps. In these conditions the hydrodynamic motion can be neglected, and we focus our attention on the ionization and heating processes. We also limit our analysis to optically transparent plasmas with the electron density smaller than the critical density. The standard laser-plasma interaction models are operational at higher electron densities.

The first step of the laser interaction with a dielectric material is the absorption of photons by electrons, leading to the electron dynamics in the solid state of matter. The first stage consists of photoionization where valence electrons are promoted to the bottom of the conduction band through multiphoton absorption or tunneling depending on both material and laser parameters. These promoted conduction electrons (or free electrons) can further absorb photons sequentially, so that they are promoted to higher energy states. When they reach an energy of the order of the band gap energy or more, their collisions with valence electrons can lead to a further ionization, the so-called impact ionization. Free electrons can also recombine to the valence band in the course of interaction. This whole dynamics can be described by multiple rate equations as [16]

$$\frac{\partial n_0}{\partial t} = \left(\frac{n_{\rm vb0} - n_{\rm fe}}{n_{\rm vb0}}\right) W_{\rm PI} + 2\left(\frac{n_{\rm vb0} - n_{\rm fe}}{n_{\rm vb0}}\right)\tilde{\alpha} n_2 - W_1 n_0 - n_0/\tau_r, \quad (1)$$

$$\frac{\partial n_1}{\partial t} = W_1 n_0 - W_1 n_1 - n_1/\tau_r, \quad (2)$$

$$\frac{\partial n_2}{\partial t} = W_1 n_1 - \left(\frac{n_{\rm vb0} - n_{\rm fe}}{n_{\rm vb0}}\right)\tilde{\alpha} n_2 - n_2/\tau_r, \quad (3)$$

where the electron population (density) n_i, with $i = 0, 1, 2$, corresponds to different energy states in the conduction band. n_0 corresponds to the bottom of the conduction band with an energy $E_k(n_0) = 0$ by convention, while $E_k(n_1) = \hbar\omega$ and $E_k(n_2) = 2\hbar\omega$. The energy of two photons is sufficient for impact ionization with our parameters of a polystyrene ablator interacting with a UV laser of $\lambda = 351$ nm, i.e., $E_{k,\max} \simeq 1.5E_g$ [16] with a band gap of $E_g = 4.05$ eV and $\hbar\omega = 3.54$ eV. For this reason three electron populations are considered. $W_{\rm PI}$ is the photoionization rate evaluated with the quantum Keldysh expression [17] which is provided in Appendix A. Such an approach is based on a temporal average over a few optical cycles, which is consistent with the present slow variations of the laser pulse envelope. The Keldysh expression accounts for both multiphoton and tunneling ionization in the solid state depending on parameters. $\tilde{\alpha}$ is the rate for collisions between free and valence electrons leading to impact ionization. Its value is in the range [10^{14} s^{-1}, 10^{16} s^{-1}] for dielectric materials [18–20]. It is weighted by a factor 2 in Eq. (1) since the collision of an electron of state 2 with a valence electron leads to the production of two electrons in state 0. To evaluate the order of magnitude of $\tilde{\alpha}$, it can be compared to the collision frequency used in the Drude model (widely used to evaluate optical properties of irradiated dielectrics by short laser pulses). The latter corresponds only to a scattering process where no significant change in the electronic structure takes place and lies generally in the range of 10^{15} s^{-1}. Since $\tilde{\alpha}$ corresponds to a more important electronic rearrangement, its probability (cross section) should be significantly smaller. We thus choose $\tilde{\alpha} = 10^{14}$ s^{-1}. W_1 is the rate for one-photon absorption in the conduction band, which evolves linearly with the laser intensity. In general, electron-phonon-photon, electron-ion-photon, and direct interband [21] processes should contribute to its value. It should also depend on the energy of free electrons. Since a precise value of W_1 for CH is unknown, we use the silica parameters for illustration purposes (band gap of roughly 8 eV) assuming that the electron dynamics in the conduction band of dielectric materials is not very sensitive to the band gap value. In Ref. [16] for $\lambda = 500$ nm, $W_1 = 3.5 \times 10^{-7} E_L^2$ in units of s^{-1}, where E_L is the laser electric field. For electron-phonon-photon collisional absorption, the rate scales as λ^4 [16] for moderate intensities. Thus, with $\lambda = 351$ nm, we set $W_1 = 10^{-7} E_L^2$. Regarding the recombination, this model assumes that electrons can recombine within a timescale set to $\tau_r = 1$ ps in accordance with standard values [20,22,23]. When going to a plasma state, the valence band is depopulated and the free electron density no longer evolves. To account for that, the coefficient $(n_{\text{vb0}} - n_{\text{fe}})/n_{\text{vb0}}$ weights the ionization rates, where $n_{\text{vb0}} = 3. \times 10^{22}$ cm^{-3} for CH is the initial electron density in the valence band, and $n_{\text{fe}} = n_0 + n_1 + n_2$ is the total free electron density. Note that we consider only single-electron ionization, involving that the maximum free electron density is limited by the atomic density, which is close to the critical plasma density ($n_c \simeq 10^{22}$ cm^{-3} for $\lambda = 351$ nm). It is sufficient for our model, which describes the transition of the ablator into the plasma state being opaque for the laser. It is worth mentioning that though several parameters and assumptions are used in this approach, they are consistent with the existing literature [24,25] that has produced accurate results.

Moving to the evaluation of the absorbed energy density, the collision frequency, ν_c, accounting for collisions of electrons with other particles has to be evaluated. It involves a momentum transfer rendering possible the photon absorption. Within the present approach, collisions with the ion-lattice are considered. In the limit cases, the solid state and the plasma state, collisions are driven by phonons and ions, respectively. The solid state is defined for not too high ion-lattice temperature, T_{il}. Here we set $T_{\text{il}} < 0.1$ eV (corresponding to a fully melted state of CH polymer). For such temperatures, collisions are mainly due to phonons. The collision frequency then is assumed to evolve as $\nu_{\text{ph}} = \nu_{\text{ph0}} T_{\text{il}}/T_0$ [26,27]. ν_{ph0} is the electron-phonon collision frequency at room temperature $T_0 = 300$ K. It is set to $\nu_{\text{ph0}} = 10^{14}$ s^{-1} [21,26–28]. This definition includes implicitly interband transitions, which were shown to provide a contribution similar to the collisional absorption for the laser heating of conduction electrons [21]. The Spitzer expression for the electron-ion collision frequency, ν_p, is used for the full plasma state [29]. We set $Z \ln \Lambda = 10$ for illustration purposes, where for temperatures of tens of eV in the plasma state, both Z and $\ln \Lambda$ are equal to a few unities. In the transition regime of electron and ion temperatures (typically in the few eV range close to the Fermi energy), the collision frequency is dominated by the mean-free path of electrons with a probability of unity for momentum transfer at each collision [30]. This upper bound for the collision frequency reads $\nu_{\text{mfp}} = v_e n_a^{1/3}$ where v_e is the electron thermal velocity and n_a the atomic density, set to 3×10^{22} cm^{-3}. For $T_{\text{il}} > 0.1$ eV, the collision frequency is evaluated by the average expression $\nu_{\text{av}}^{-1} = \nu_{\text{mfp}}^{-1} + \nu_{e-i}^{-1}$, which is an interpolation between both asymptotic regimes.

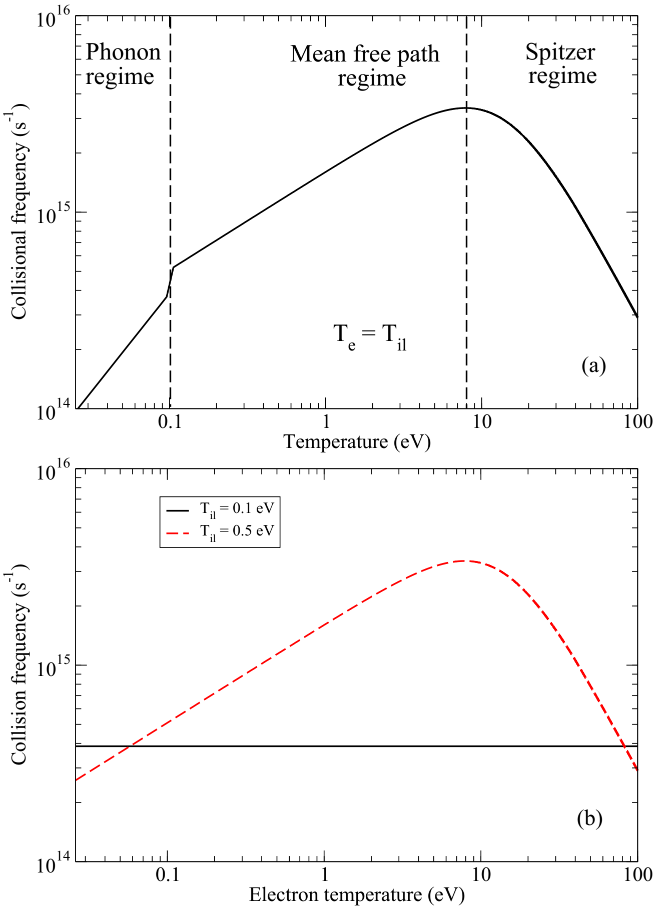

FIG. 1. Evolution of the collision frequency as a function of electron temperature in (a) the equilibrium case ($T_e = T_{\text{il}}$) and (b) for two constant ion-lattice temperatures of 0.1 eV and 0.5 eV. In all cases $n_{\text{fe}} = 10^{22}$ cm^{-3}.

The evolution of this collision frequency as a function of temperature, assuming the equilibrium $T_e = T_{\text{il}}$ and $n_{\text{fe}} = 10^{22}$ cm^{-3}, is plotted in Fig. 1(a). Despite the following results $T_e > T_{\text{il}}$, this case is chosen for illustration purposes allowing us to exhibit all regimes at a glance. The vertical dashed lines separate the various regimes. Standard trends are retrieved [30] including the transition to the full plasma state for a temperature of the order of 10 eV. Note that the discontinuity in the collision frequency at 0.1 eV is due to our stringent definition of the criterion to leave the solid state (phonons are removed above the melting temperature). Such a transition is obviously smoother but takes place in a rather narrow range of temperatures. Without changing the main conclusions of this work, we thus have chosen to keep this simple description. Figure 1(b) shows the evolution of the collision frequency with respect to the electron temperature for $T_{\mathrm{il}} = 0.1$ eV and $T_{\mathrm{il}} = 0.5$ eV. In the first case, the collision frequency is constant since the matter is in the solid state. In the second case where the solid phase is removed, a similar behavior as the one of Fig. 1(a) is retrieved.

In order to determine the electron and ion-lattice temperatures, T_e and T_{il}, the two-temperature model is used [31]. By neglecting the transport on the present 100 ps timescale for now (when the model is implemented into hydrocodes, the thermal conduction can be taken into account), this model reads

$$C_e \frac{dT_e}{dt} = \frac{dU}{dt} - \frac{3}{2} k_B \frac{dn_{\mathrm{fe}}}{dt} T_e - G(T_e - T_{\mathrm{il}}), \tag{4}$$

$$C_{\mathrm{il}} \frac{dT_i}{dt} = G(T_e - T_{\mathrm{il}}). \tag{5}$$

Compared to the two-temperature model for metals, the additional term $\frac{3}{2} k_B \frac{dn_{\mathrm{fe}}}{dt} T_e$ accounts for the temporal evolution of the electronic heat capacity (due to the evolution of the free electron density). The heat capacities are $C_e = 3n_{\mathrm{fe}} k_B/2$ and $C_i = 3n_a k_B/2$. These values pertain to temperatures of at least a few eV, which are reached relatively early during the interaction. The electron-ion energy exchange factor G is evaluated by $G = C_e \nu_c m_e/m_{\mathrm{il}}$. The electron to ion mass ratio weights the collision frequency to account for energy exchange (ν_c accounts for momentum transfer). We set $m_e/m_{\mathrm{il}} = 1/1836$ accounting for the fact that hydrogen atoms in CH mainly ensure the energy transfer. Doing so, we have checked that, after a fast (<1 ps) energy absorption in a solid state, the equilibrium is reached from a few to 10 ps, which is a correct order of magnitude [20,25]. The absorbed laser energy density per unit of time, $\partial_t U$, is described with the Joule heating term $\partial_t U = \vec{j} \cdot \vec{E}_L$ where $\vec{j}$ is the electron current density. By using the Ohm law, $\vec{j} = \sigma \vec{E}_L$ and the Drude model to evaluate the conductivity, $\sigma = \sigma_0/(1 - i\omega\nu_c^{-1})$ with $\sigma_0 = e^2 n_{\mathrm{fe}} \nu_c^{-1}/m_e$, one obtains

$$\frac{\partial U}{\partial t} = \frac{e^2 n_{\mathrm{fe}} \nu_c}{m_e(\omega^2 + \nu_c^2)} E^2. \tag{6}$$

To account for the laser propagation and predict the energy deposition along the direction of laser propagation, within the present conditions of relatively long time and spatial scales, a full Maxwell solver cannot be used due to its computational cost. Maxwell equations thus have to be simplified. First, we use the paraxial approximation consisting in neglecting second-order derivatives. Since we consider the region of a laser speckle, the beam is mainly parallel in the interaction region, and the propagation equation reduces to the Beer-Lambert law:

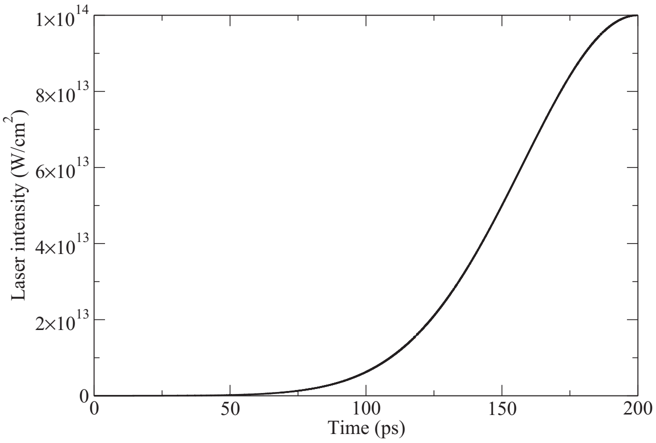

FIG. 2. Evolution of the laser intensity as a function of time. The second part of the pulse is not shown because simulations are stopped before.

$$v_g \frac{\partial I}{\partial z} = -\nu_c I - \left(\frac{n_{\mathrm{vb0}} - n_{\mathrm{fe}}}{n_{\mathrm{vb0}}}\right) W_{\mathrm{PI}} E_g \tag{7}$$

with $v_g = c\sqrt{1 - n_{\mathrm{fe}}/n_c}$, c being the speed of light in the matter. The first term on the right-hand side accounts for the collisional absorption. The second one is for the photoionization. By solving this equation for each time step, the temporal profile of the laser pulse and radial profile of the speckle are accounted for. It is worth noting that Eq. (7) remains valid as long as the electron density is lower than the critical plasma density. If not, the laser pulse can be reflected in the critical density, and Eq. (7) thus does not apply.

III. MODELING RESULTS AND DISCUSSIONS

A. Temporal evolutions of physical quantities on the target surface

The aim of this section is to demonstrate the reliability of the model for the electron dynamics, the absorbed energy, and the temperature evolution, by exhibiting values of these quantities which are reasonable. For that purpose, the laser propagation is not included, corresponding to considering the dynamics on the target surface.

To perform simulations with the model presented in Sec. II, the used temporal intensity profile is shown in Fig. 2. It consists of a Gaussian shape $I(t) = I_0 \exp(-4\ln 2\,(t - t_{\max})^2/\tau^2)$ with a duration of $\tau = 100$ ps, or $\tau_{\mathrm{FWHM}} = \tau/2\sqrt{\ln 2}$ the full width at half maximum (FWHM); and we set $t_{\max} = 200$ ps. The maximum intensity is $I_0 = 10^{14}$ W/cm^2. Such an intensity profile is relevant of the pickets used in ICF experiments to conditioning the target [32]. For intensities in the 10^{13} W/cm^2 range, the photoionization rate is already large so that a full ionization is expected [17,25]. The simulations are thus stopped around $t \simeq 100$ ps where an overcritical plasma state ($n_e > n_c$) is expected to be already formed. Also note that this relatively large photoionization rate removes any influence of an initial free electron density. Indeed, the latter is of the order of 10^8–10^{10} cm^{-3} [33], which is much smaller than densities induced by photoionization

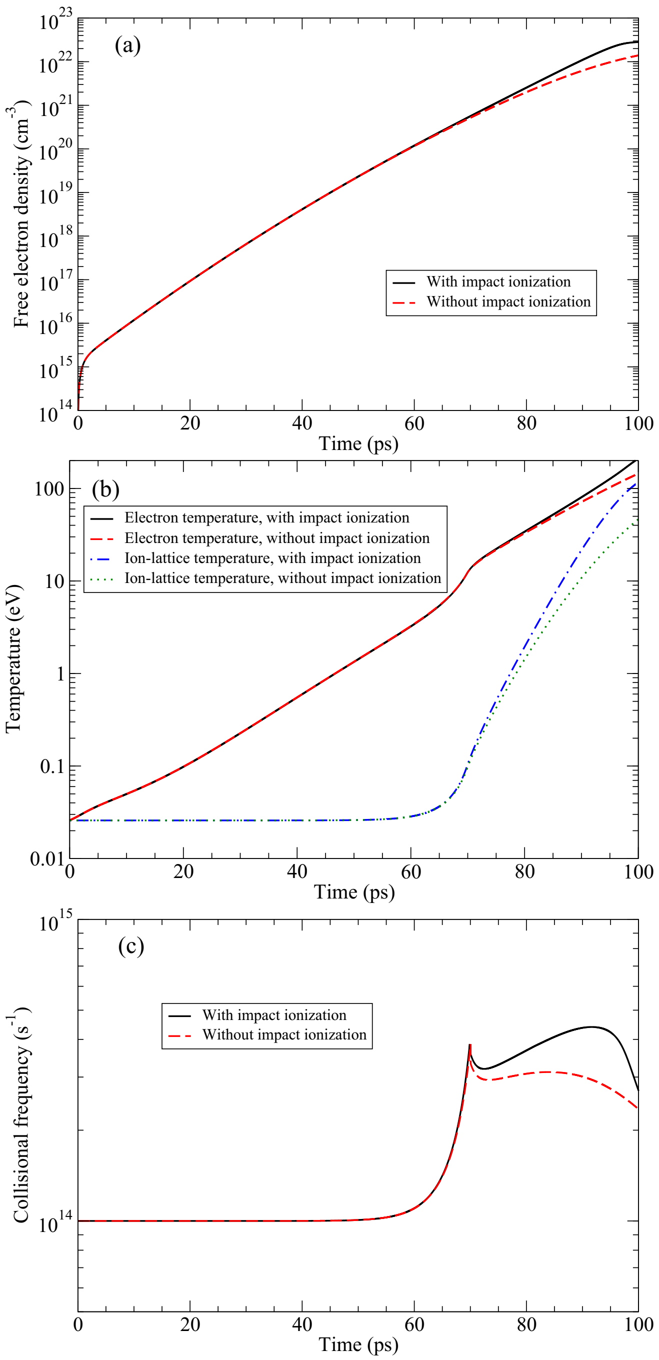

FIG. 3. Evolution of (a) the electron density, (b) the temperatures, and (c) the collision frequency as a function of time on the front surface ($z = 0$).

which quickly reach values many orders of magnitude larger, as shown in Sec. III A and Appendix B.

Figure 3 shows the temporal evolution of (a) the free electron density, (b) both the electronic and ion-lattice temperatures, and (c) the collision frequency at the target front surface ($z = 0$) with all previously defined parameters. In all cases, the impact ionization process is taken into consideration or not in order to highlight its influence on the overall system dynamics. Regarding the electron density, without impact ionization, it evolves exponentially up to roughly 100 ps. This evolution follows the Gaussian shape of the laser pulse. After this time, the density saturates and reaches the maximum allowed value of n_a within this model. When the impact ionization is switched on, a departure from the previous case is observed at 80 ps or so. At this time, the electron avalanche engages, leading the density to reach the maximum value in a shorter timescale, i.e., slightly before 100 ps. In particular the exponential behavior stands up to the saturation.

Due to the collisional absorption, following the electron density evolution, the electron temperature increases exponentially from 25 meV (300 K) to around 100 eV on the 100 ps timescale. In that case, temperatures are such that a plasma state is reached where the collision frequency decreases with respect to the electron temperature as shown in Fig. 3(c). As for the density, the electron temperature is lower when the impact ionization is switched off. Indeed, a smaller electron density leads to a smaller absorbed energy density. For such electron temperatures, electron-ion collisions may lead to multiple ionization, thus decreasing the temperature variations. Note that the slope has a discontinuity at $t \simeq 70$ ps. This is the signature of a change in the matter state where the electron-phonon collisions are replaced by the electron-ion collisions. This transition is well observed on the evolution of the collision frequency at $t \simeq 70$ ps.

Regarding the ion-lattice temperature, as long as the electron temperature is not high enough, it remains close to the room temperature. It starts to increase when the electron temperature is of the order of 10 eV at $t \simeq 70$ ps. It then grows exponentially as the electron temperature rises. This behavior is driven by the increase in the collision frequency due to the rise in the electron temperature. At $t \simeq 70$ ps, this increase is such that the electron-ion coupling (driven by the value of G [Eq. (5)] becomes sufficiently large to induce a departure of the ion-lattice temperature from the initial room temperature. As for the electron temperature, the impact ionization leads to higher ion-lattice temperatures but its influence is lost for the longest times. A break in the slope also appears at $t \simeq 70$ ps, which indeed corresponds to $T_{\text{il}} = 0.1$ eV, i.e., the matter starts to undergo the solid-to-plasma transition.

The evolution of the collision frequency as shown by Fig. 3(c) confirms the previous trends. As long as the solid state stands, it increases. Due to the first phase transition around 70 ps, the collision frequency evolution then is governed by the mean-free path of electrons. It thus still continues to increase from a lower value (imposed by the state change) due to the electron temperature rise. Finally, it decreases when the plasma state is mainly reached where the Spitzer regime stands. Regarding the influence of the impact ionization, between 70 ps and 100 ps, it leads to higher collision frequency since both electron density and temperatures are larger.

The following trends can be deduced from the previous study: (1) the electron temperature evolution is similar to the laser intensity envelope, (2) the ion-lattice remains cold during a relatively long period of time, its temperature increases strongly only when the matter is entering the plasma state, (3) photoionization dominates up to high densities of the order of $0.1n_c$, only after the electron avalanche driven by the impact ionization engages. Such behaviors have already been reported in similar conditions [25], which makes the present modeling reliable. Note that the modeling parameters have been set to reasonable values also in accordance with the current state of the art. Similar trends are expected by slightly varying the value of the modeling parameters. Also note that some of the used parameters may evolve with respect to the state of matter. Since there is no modeling to describe this evolution to our knowledge, they are set to the previous reasonable constant values for now.

From the previous numerical results, we conclude that the 100-ps timescale for the solid-to-plasma transition corresponds to the moment where the free electron density is reaching the critical plasma density. This condition is a standard criterion to define a material phase transition [19,26]. Indeed, the associated increase in the collision frequency then leads to relatively high electron temperatures and efficient electron-ion coupling. The ion-lattice temperature then also increases significantly leading rapidly to the plasma state. Note that 100 ps is the order of magnitude and not an exact value since numerical simulations are performed with an arbitrary initial time such that the laser intensity is small enough to guarantee no significant material ionization. In order to understand more clearly the timescale origin of the solid-to-plasma transition, evaluate more precisely its value, and exhibit how it depends on the laser parameters, an analytical expression is derived in Appendix B for any temporal pulse shape. For a Gaussian intensity envelope, the transition timescale reads

$$\Delta t_t = \tau_{\mathrm{FWHM}}\left(\sqrt{\ln\left[I_0\sqrt{\frac{\tau_{\mathrm{eff}}\sigma_2}{n_i}}\right)} - \sqrt{\ln\left(I_0\sqrt{\frac{\tau_{\mathrm{eff}}\sigma_2}{n_c}}\right)}\right], \tag{8}$$

where I_0 is the maximum intensity, σ_2 is the generalized two-photon ionization cross section (the general Keldysh expression here is used in the limit case of pure multiphoton absorption; see Appendix A), $n_i = 10^{10}$ cm^{-3} is the intrinsic free electron density before any irradiation, and τ_{eff} is an effective characteristic time. Without and with impact ionization, $\tau_{\mathrm{eff}} = \tau_r$ and $\tau_{\mathrm{eff}} = (\tau_r^{-1} - \beta)^{-1}$, respectively. β can be written as $\beta = \sigma I$ where σ is of the order of one to a few cm^2/J within the present conditions. The expression (8) shows the parameters which drive the evolution of the transition timescale. Their influence is obvious: because $n_c \gg n_i$, the larger I_0, σ_2, or τ_{eff}, the shorter Δt_t.

With the present laser parameters, without impact ionization, $\Delta t_t \simeq 140$ ps, which is in a good agreement with what is observed numerically. Note that due to the fact that Δt_t is a very slowly varying function, changing the value of n_i or τ_{eff} even by a few orders of magnitude does not change significantly the timescale. For instance, always by changing the value of one parameter, $\Delta t_t \simeq 156$ ps with $n_i = 10^8$ cm^{-3}, $\Delta t_t \simeq 130$ ps with $\tau_r = 10$ ps, and $\Delta t_t \simeq 123$ ps with $I_0 = 10^{15}$ W/cm^2. When the impact ionization is included, with $\sigma = 1$ cm^2/J and $I = 10^{12}$ W/cm^2, $\beta = 10^{12}$ s^{-1}, which is of the order of τ_r. Taking $\tau_{\mathrm{eff}} = 100$ ps for illustration purposes where the impact ionization almost compensates the recombination, the transition timescale is about 123 ps. Two orders of magnitude in τ_{eff} thus change the timescale only by about 10%. This small sensibility is due to the logarithmic behavior of the timescale with the involved parameters, which is consistent with the results of Fig. 3. These timescale values are consistent with numerical simulations (not shown), which also validates the analytical approach.

Actually, for a temporal Gaussian intensity shape, this is the laser pulse duration, which mainly imposes the timescale for the solid-to-plasma transition as shown by Eq. (8). Obviously another temporal shape would lead to a different sensibility with respect to the parameters. A linear intensity profile would provide a stronger dependence on the maximum intensity, for instance, and a different timescale. In all cases, the phase transition is achieved when the intensity reaches $I_c = \sqrt{n_c/\sigma_2\tau_r}$ (see Appendix B). Overall, the 100-ps transition timescale pertains to realistic conditions in terms of material parameters and laser parameters including the pulse shape and the maximum intensity.

The previous considerations have shed light on the dynamics of the ablator at the target front surface. The influence of the phase transition of the irradiated matter has been shown in particular. These evolutions in the target volume are now addressed in the following section.

B. Laser propagation through the target bulk

The objective of this section is to evaluate the bulk heating of the ablator before a full ionization takes place and plasma becomes opaque for the laser radiation.

The simulations performed in this section use the same model and parameters as previously, but the laser propagation through the material is now included by further solving Eq. (7). To be consistent with the current direct drive ICF design [32], the thickness of the CH shell is chosen to be $z_{\mathrm{max}} = 8$ μm. The evolutions of the laser intensity, the electron temperature, and the collision frequency as a function of both time and propagation distance z are provided in Fig. 4. Regarding the laser intensity, at any instant, it decreases with respect to the propagated distance due to the absorption. However, the larger the laser intensity on the front surface (at a given time), the larger the intensity variations along the propagation axis. This behavior is due to the nonlinear evolution of the induced free electron density with respect to the intensity: the larger the intensity, the larger the ionization rate, and thus the stronger the laser absorption. That results in an almost constant intensity with respect to time at $z = 8$ μm, close to 1 TW/cm^2 (for $t > 70$ ps). This value corresponds to the ionization threshold as was discussed in the context of the so-called "shine-through" problem [13]. The two-photon absorption cross section is so small for intensities lower than this threshold that the produced electron density is not sufficient to affect the laser propagation (in terms of absorption due to ionization or heating of the free electrons). In addition, for such moderate intensities, the impact ionization rate is not large enough to engage an electron avalanche process [34].

The same trends are also observed for the electron temperature since it is roughly proportional to the electron density, the latter being a monotonic function of the laser intensity. Also the longer the propagation distance, the smaller the temperature; the longer the time (in the pulse), the stronger the temperature variations along the ablator thickness. When the critical density is reached ($t \simeq 90$ ps), the temperature drops from 100 eV on the front surface to a few tens of eV on the rear surface at $z = 8$ μm, whereas it is almost constant, on the order of a few eV to 10 eV, at $t \simeq 60$–70 ps.

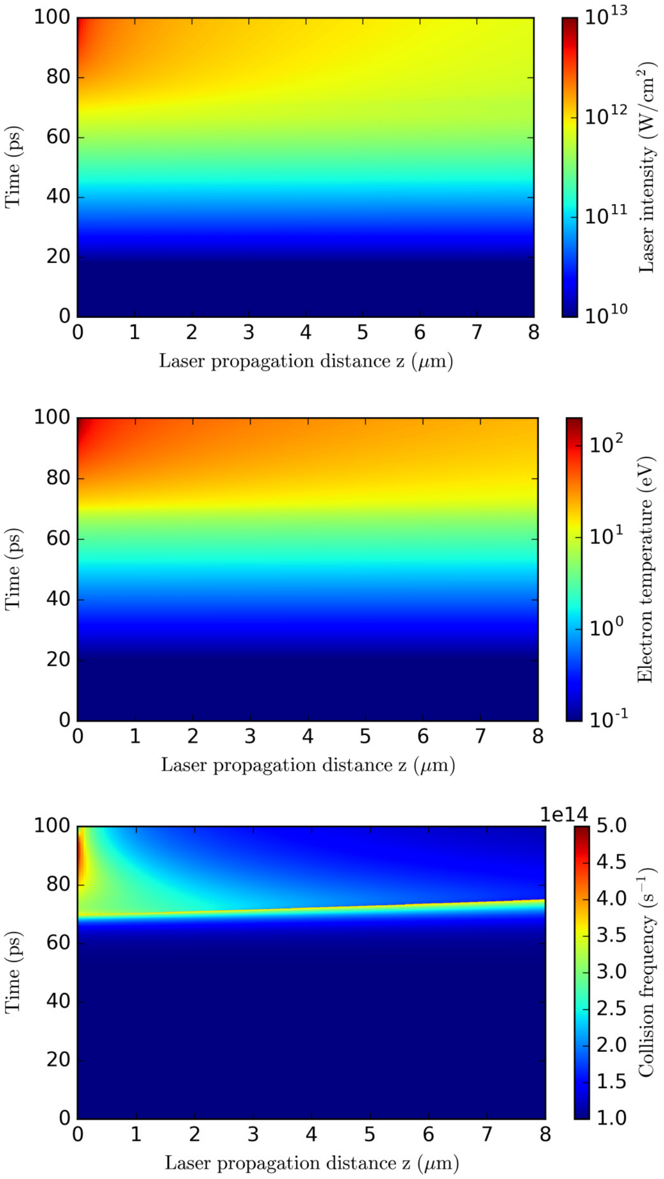

FIG. 4. Contour plots of laser intensity (top), electron temperature (middle), and collision frequency (bottom) as a function of time and the laser propagation axis z. The laser starts at $z = 0$ (target surface) and propagates along the z direction.

The latter behavior is in part due to the collision frequency, which remains the largest for $t \simeq 70$–80 ps along the whole propagation axis. For those times, both the temperature and the collision frequency have increased, but the ion-lattice temperature remains lower than the melting temperature. Considering the whole behavior of the collision frequency, similar trends with respect to time as presented in the previous section are retrieved whatever the traveled distance. However, above $z = 2$ μm, after reaching the peak, it decreases slower with time compared to the behavior close to the front surface. This is due to the fact that temperatures are smaller. The absorption thus remains efficient, leading to a further decreasing channel for the intensity (in addition to the nonlinear absorption process). This overall explains why the variations in the various physical quantities are the smallest with respect to time for the longest traveled distances, and the smallest with respect to the distance for the shortest times: the present nonlinear system steers a smoother variation for the physical quantities for sufficiently long traveled distances or times.

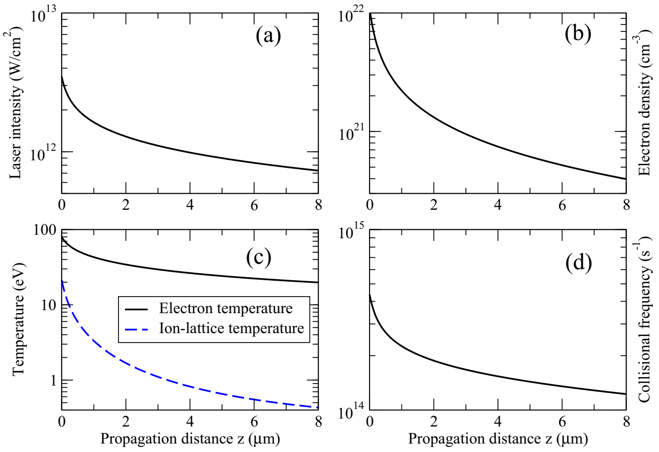

FIG. 5. At $t = 90$ ps, evolution of (a) the laser intensity, (b) free electron density, (c) electron and ion-lattice temperatures, and (d) collision frequency as a function of the propagation distance z.

To get more quantitative estimates and insights into the ICF conditions, cuts of the previous graphs are presented in Fig. 5. It shows the evolution of (a) the laser intensity, (b) the free electron density, (c) the electron and ion-lattice temperatures, and (d) the collision frequency as a function of the propagation distance at $t = 90$ ps (when the critical density is reached on the front surface). All presented quantities decrease monotonically and regularly with respect to the propagation distance. In that case, the laser intensity on the front surface, close to 3 TW/cm^2, is sufficiently small to ensure the same regime whatever the traveled distance: the electron density saturation is not reached, and the induced temperatures are relatively small so that their variations are not too much important. In the course of propagation, the laser intensity decreases smoothly due to the absorption by the electrons. The free electron density thus also decreases due to lower intensities. The electron temperature thus follows the same trend. However, its variations are less important since it is mainly driven by the collision frequency through the absorbed energy density U (despite that U also includes the free electron density, its influence on the temperature is mainly canceled by the heat capacity, which scales linearly with the electron density). Indeed, the collision frequency decreases by only a factor of 4 because, in the Spitzer regime, its decrease imposed by the density is compensated by the decrease in temperature. Overall, the monotonic decrease in the collision frequency is mainly driven by the decrease in electron density.

IV. POSSIBLE CONSEQUENCES ON THE INTERNAL STRUCTURE OF THE TARGET

A. Consequences of the laser imprint on the CH ablator

The laser imprint results from spatial laser inhomogeneities (speckles) which induce density and temperature gradients. The associated pressure thus leads to nonuniform deforma-

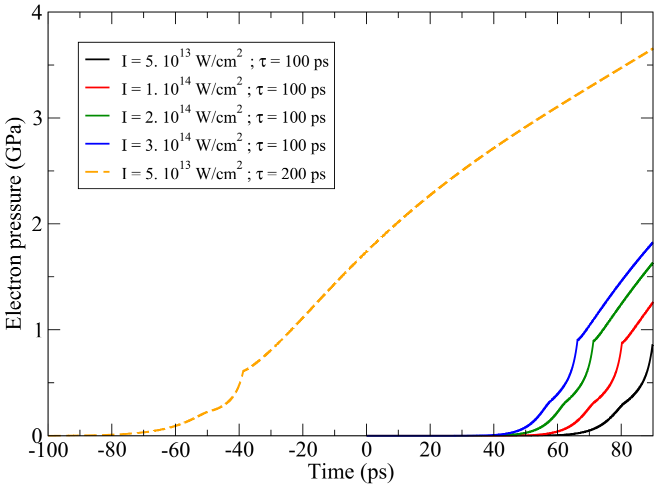

FIG. 6. Evolution of the electron pressure as a function of time at $z = 8\ \mu m$ in the center of a speckle. Various laser parameters are used.

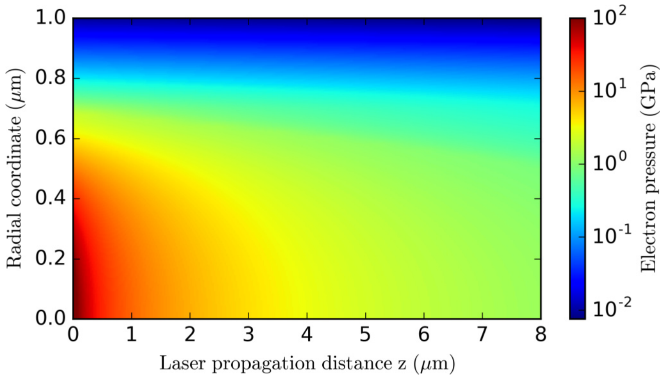

FIG. 7. Evolution of the electron pressure as a function of the laser propagation distance z and the radial coordinate of a speckle, at $t = 90$ ps. The maximum intensity in space and time is 10^{14} W/cm^2.

tions of both the CH shell and the CH-DT interface. Such nonuniformities provide a seed to the development of RT instabilities. To evaluate the transverse deformations, the one-dimensional description can be augmented to a two-dimensional description through the following simple considerations. Since the ablator thickness is comparable to the speckle length (for a speckle width of 1 μm, the Rayleigh length is roughly 10 μm, which is larger than the ablator thickness), a straightforward laser propagation can be considered, with negligible transverse losses. Then, knowing the intensity transverse profile at the entrance $z = 0$, we can restitute the temperature and pressure profiles at the rear side ($z = 8\ \mu$m) by solving Eq. (7) for various radial positions. Then an ideal gas equation of state is used to get a first estimation of the electron pressure. Note that the ion-lattice pressure becomes equivalent when the temperature equilibrium is reached.

We first study the temporal evolution of the electronic pressure at $z = 8\ \mu m$ (the back surface of the CH shell) for various laser parameters. For the previous pulse duration, $\tau = 100$ ps, the electronic pressure temporal evolution at $z = 8\ \mu$m for various maximum intensities is provided by Fig. 6 (corresponding to the center of a speckle). The onset of the pressure growth takes place earlier for higher intensities. The pressure then increases almost linearly with respect to time. And as expected, the higher the laser intensity, the larger the pressure. However, by varying the intensity by a factor of 6, the pressure varies only by a factor of 2. This small dependence on the intensity has been discussed previously. Within the present conditions, electronic pressure induced by a speckle is expected to be of a few GPa, which is enough to induce significant deformations at the CH-DT interface in a direct drive ICF target. Note that for the highest intensities and longest times, the pressures are slightly overestimated since the critical density is reached.

To further exhibit how a laser speckle may imprint the target, a transverse direction to the laser propagation axis now is further considered. We assume a cylindrical symmetry, r being the radial coordinate, where each physical processes at a given r are independent of those of other radial position. This assumption is reliable if the transverse gradients of the electron density in particular are sufficiently small. The laser intensity profile thus should be relatively smooth, which is the case with a Gaussian spatial profile of a speckle. The radial distribution of the various considered physical quantities are then obtained by performing the previous calculations, with some intensities relevant of the radial speckle distribution, independently from each other.

The following results have been obtained with a speckle size of 1 μm FWHM, i.e., $\simeq 3\lambda$, and a maximum intensity in the speckle center of 10^{14} W/cm^2. Figure 7 shows the evolution of the electron pressure with respect to both the propagation distance and the radial coordinate at $t = 90$ ps. Note that results for pressure higher than 100 GPa are not shown to highlight the behaviors in the interface region around $z = 8\ \mu$m. Figure 7 shows a high-pressure region on the front surface which decreases along the radial direction as the laser intensity does. In the center of the speckle, the longer the propagation distance, the smaller the pressure. On the speckle edge, due to the threshold effect induced by nonlinear processes as discussed previously, the induced pressure is small (0.1 GPa) and is almost constant along the longitudinal coordinate. This results in strong pressure gradients on the front surface and relatively smooth on the interface. Such transverse pressure modulations may generate strong transverse acoustic waves with an amplitude depending on the longitudinal position z (strong acoustic waves and no shock is expected in the transverse direction since the matter flow velocity $\sqrt{\Delta P/\rho} \simeq 1$ km/s is of the order of the sound speed). These acoustic waves may thus induce a local shearing of the plastic shell which may be detrimental for the subsequent implosion.

To further quantify these results on the interface, Fig. 8 shows the radial evolution of the pressure at $t = 90$ ps within the same conditions as previously. The renormalized (to the maximum pressure at $r = 0$) speckle intensity profile is also plotted as a reference. Despite the pressure decreases monotonically, two main regions can be observed. In the inner part ($r < 0.5\ \mu$m), it is flatter than the intensity profile due to the above-mentioned smoothing influences. For longer radius, first a discontinuity in the slope can be observed which

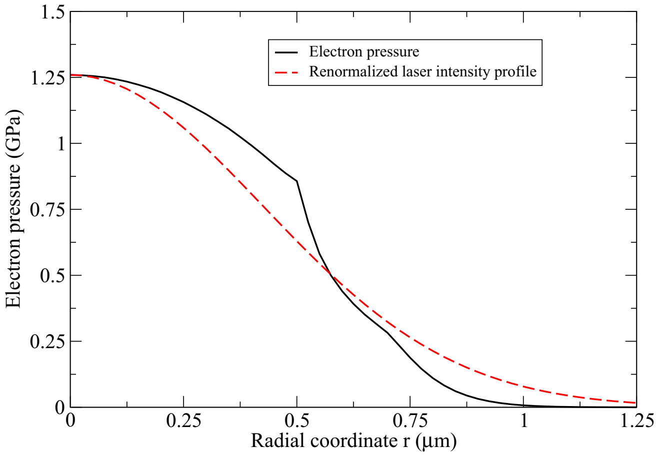

FIG. 8. At $t = 90$ ps on the CH-DT interface ($z = 8\ \mu$m), evolution of the electron pressure as a function of the radial coordinate. The maximum incident intensity in time and space is 10^{14} W/cm^2.

corresponds to conditions where the intensity is close to the previously discussed threshold of 1 TW/cm^2. Crossing this intensity, the electron dynamics behavior becomes significantly different. The pressure then drops faster than the laser intensity with respect to the radial distance. It turns out that the pressure variations does not follows those of the intensity, which is consistent with recent observations of the amplitude of shock velocity nonuniformity due to laser inhomogeneities [12].

In order to control these deformations, the laser parameters can be optimized. Here we consider a constant fluence. The case $I_{\max} = 10^{14}$ W/cm^2 and $\tau = 100$ ps is used as a reference. Calculations have been performed for $I_{\max} = 5 \times 10^{13}$ W/cm^2 and $\tau = 200$ ps providing the same fluence as the reference case. The resulting pressure is shown in Fig. 6 where the origin of time is defined such that, whatever the pulse duration, the maximum intensity is reached at $t_{\max} = 200$ ps. Compared to the reference case, obviously the onset takes place earlier for the 200 ps pulse duration. The slope is smaller, but since more time is allowed for heating the electron system, the final pressure is larger by a factor of ~2. It thus appears that, for a given fluence, shorter picket pulses are desirable.

The amount of energy of a laser picket which shines through the CH to the fuel then can be estimated from the present calculations. We have shown that the CH shell is mainly transparent for laser intensities lower than roughly 1 TW/cm^2. Assuming the DT fuel consists of a shell of thickness of ~50 μm with a radius of ~400 μm, an uniform irradiation with the threshold intensity during 100 ps corresponds to ~0.7 J injected in the target. Due to the fact that several laser beams superpose inside the target, local intensities can be in excess of the threshold intensity, leading to a further absorption of the shine-through irradiation by the inner part of the CH ablator. Assuming that only 10% of this shine-through energy is absorbed uniformly in the ablator, the associated energy density is ~3 kJ/cm^3, leading to a temperature increase of the order of ~2000 K. Such an influence may lead the ablator to melt before the main laser pulse arrives, which could be detrimental for the ICF scheme as explained in more details in Sec. IV B.

All the previous considerations have described the evolution of matter up to conditions where the critical plasma density is reached in order to ensure the reliability of the present modeling. This condition corresponds to the early formation of a plasma state at solid density or the so-called warm dense matter. Once this state is reached, with an electron density larger than the critical one, the laser reflection takes place in the vicinity of the front target surface. It is associated with a significant hydrodynamic expansion in the speckle irradiation region and a launch of longitudinal shock waves inside the ablator. Interaction of the shock with transverse acoustic waves then may shear the CH-DT interface.

B. Consequences on the DT fuel

The previous estimations allow us to draw conclusions regarding the integrity of the DT fuel following this early stage of the solid to plasma formation. The direct shine-through irradiation should not have any influence on the solid DT since its band gap is in excess of 10 eV. Indeed, at least three photons are required to ionize the solid DT, the ionization rate is thus negligible with laser intensities of the order of 1 TW/cm^2. The melting of the CH ablator at the CH-DT interface, due to the shine-through irradiation, may be a first cause of loss of integrity of the DT fuel. Indeed due to heat conduction through the interface (the characteristic length of heat diffusion $2\sqrt{D\Delta t}$ in solid DT within 1 ns is shorter than 1 nm), the DT ice may start to undergo a phase transition at the interface before the main laser pulse arrives. That may results in a detachment of the CH shell from the ablator. Another detrimental effect could be due to the induced pressure by a laser speckle at the interface. First, the pressure gradient on the steep interface may deform it locally. Second, due to the spatial interface discontinuity, a shock wave (with moderate amplitude in the GPa range) is expected to be launched towards the DT fuel. The shock entropy of the order of 5 kJ/g is 10 times larger than the DT latent heat. It may lead to the fuel melting or vaporization. The laser interaction with the CH ablator may also induce a Bremsstrahlung irradition [35], leading to a further heating of the DT fuel through linear absorption. All these processes may lead the initial solid DT to expand at some places due to local phase transitions (inducing pressure gradients in the fuel). Generation of cracks could also be possible on the nanosecond timescale before the main laser pulse arrives since the shear strength of solid DT is only of the order of 1MPa. These processes could be responsible for the loss of integrity of the solid DT fuel; they need to be thoroughly analyzed to provide the best ICF conditions.

V. CONCLUSION AND OUTLOOKS

In current state-of-the-art hydrocodes to simulate the inertial confinement fusion, a plasma state is assumed at the beginning of the interaction. All properties pertaining to the solid state of the ablator and fuel, as the insulating property, are not taken into consideration. For instance, the early absorption is modeled with inverse Bremsstrahlung whereas it is due to nonlinear processes as the multiphoton absorption resulting in electron transitions from the valence band to the conduction band of dielectric materials. Such current modeling may lead one to overestimate the early absorption and lead to spurious hydrodynamic behaviors or miss the energy deposition which takes place deeper in the ablator, leading to incorrect predictions.

A model for the solid-to-plasma transition within the inertial confinement fusion framework has thus been developed for the first time. The main required ingredients have been used: electron dynamics in the solid state, absorption depending on the matter state (going from phonon assisted to ions), two-temperature model, and laser propagation. As a first modeling attempt within this context, the model is simplified by two assumptions: the hydrodynamic motion is neglected, and the free electron density is limited by the critical plasma density. Despite its simplicity, this model allows us to draw major conclusions: (1) roughly 100 ps are required to induce a full plasma state in the speckle area of a laser picket, suggesting the current hydrocodes have to account for the solid-to-plasma transition to make reliable predictions, (2) the spatial profiles of temperatures and pressures are influenced by early nonlinear absorption processes, and (3) detrimental effects of the initial solid state can be expected: local compression and shearing of the ablator and non-negligible preliminary local heating of DT fuel, which may render inefficient the target design.

The present approach can be further extended by coupling it to a hydrodynamic code: it is not computationally time-consuming and could be easily adapted to model the laser propagation and energy deposition. Indeed the present approach of laser energy lost along a direction can be straightforwardly adapted to a curved trajectory as obtained within the standard geometrical optics, i.e., the ray tracing technique, or its complex version which allows us to know well the laser intensity [36], which is mandatory to evaluate the rates of the nonlinear processes. The present model to describe the absorption during the solid-to-plasma transition is thus expected to be reliable on long timescale. Overall, work dedicated to determining the conditions to switch between the present model and the standard inverse Bremsstrahlung absorption will have to be addressed. When such developments are available, the major conclusions of the present work should be revisited in order to get more quantitative trends on longer timescales pertaining to cases of interest for ICF applications.

ACKNOWLEDGMENTS

G.D. thanks Patrick Mora for a fruitful discussion of the collisional absorption. Stéphane Coudert is also acknowledged for helping to make the contour plots with Python software. This work has been carried out within the framework of the EUROfusion Consortium and has received funding from the Euratom research and training programme 2014-2018 under grant agreement No. 633053. The views and opinions expressed herein do not necessarily reflect those of the European Commission. This work was partially supported by the project ELITAS (ELI Tools for Advanced Simulation) CZ.02.1.01/0.0/0.0/16_013/0001793 from the European Regional Development Fund.

APPENDIX A: EXPRESSION OF THE PHOTOIONIZATION RATE

An expression of the photoionization rate was derived by Keldysh [17]. It reads

$$W_{\mathrm{PI}} = \frac{2\omega}{9\pi}\left(\frac{\omega m^*}{\hbar\gamma_1}\right)^{3/2} Q(\gamma, x) \times \exp\left[-\pi\langle x+1\rangle \frac{K(\gamma_1)-E(\gamma_1)}{E(\gamma_2)}\right], \tag{A1}$$

where the symbol $\langle x\rangle$ denotes the integer part of the number x, and $\gamma = \omega\sqrt{m^* E_g}/eE_l$ is the Keldysh parameter. E_g is the band gap, E_l the laser electric field, $m^* = m_e/2$ the electron reduced mass, e the electron charge, and ω the laser frequency. The functions K and E are the complete elliptic integrals of the first and second kinds, respectively. $\gamma_1 = \gamma/\sqrt{1+\gamma^2}$ and $\gamma_2 = \gamma_1/\gamma$. The function $Q(\gamma, x)$ in Eq. (A1) reads

$$Q(\gamma, x) = \sqrt{\frac{\pi}{2K(\gamma_2)}} \sum_{n=0}^{\infty} \exp\left[-\pi n \frac{K(\gamma_1)-E(\gamma_1)}{E(\gamma_2)}\right] \Phi\left[\pi\sqrt{\frac{2\langle x+1\rangle - 2x + n}{2K(\gamma_2)E(\gamma_2)}}\right], \tag{A2}$$

where $\Phi(z) = \int_0^z \exp(y^2 - z^2)\,dy$ and $x = \tilde{E}_g/\hbar\omega$. $\tilde{E}_g$ is the effective band gap given by

$$\tilde{E}_g = \frac{2U}{\pi\gamma_1} E(\gamma_2). \tag{A3}$$

We have checked that within the conditions used in this work, the Keldysh parameter is still larger than unity so that the multiphoton absorption regime always stands. Thus the photoionization rate can be written in a simpler form $W_{\mathrm{PI}} \simeq \sigma_2 I^2$ where σ_2 is the generalized two-photon absorption cross section. From the Keldysh expression, we get $\sigma_2 \simeq 7 \times 10^8$ cm s/J^2.

APPENDIX B: ANALYTICAL EXPRESSION FOR THE SOLID-TO-PLASMA TRANSITION TIMESCALE

Here is derived an analytical expression to evaluate the timescale for the solid-to-plasma transition. This timescale corresponds to the instant where the critical plasma density is reached, then leading to a very strong absorption, fast temperature rise, and thus a phase transition. The analysis presented in Sec. III A shows that the photoionization process mainly contributes to this timescale (see Fig. 3). The impact ionization contributes only when the free electron density is large enough, and then the critical plasma density is reached quickly, i.e., in 10 ps, which is 10% of the 100 ps timescale. As a first step the impact ionization is thus neglected in the electron dynamics. Equation (1) thus reads

$$\frac{\partial n_{\mathrm{fe}}}{\partial t} = W_{\mathrm{PI}}(t) - n_{\mathrm{fe}}/\tau_r, \tag{B1}$$

where $(n_{\mathrm{vb0}} - n_{\mathrm{fe}})/n_{\mathrm{vb0}}$ is assumed to remain of the order of unity because we are here interested only in free electron densities significantly smaller than n_{vb0}. The dependence on time of the photoionization rate is due to the temporal intensity evolution. The exact solution of Eq. (B1) is

$$n_{\mathrm{fe}}(t) = n_i + e^{-t/\tau_r}\int_{-\infty}^{t} dt' W_{\mathrm{PI}}(t') e^{t'/\tau_r}, \tag{B2}$$

where n_i is the initial free electron density, i.e., before any irradiation. It is of the order of $n_i = 10^8$–10^{10} cm^{-3} [33]. The expression of the photoionization rate is relatively complicated so that it cannot be integrated, especially with a temporal Gaussian profile for the laser intensity. To evaluate the integral of Eq. (B2), the quasistationary approximation can be used. Indeed, the integral can be developed as

$$\int_{-\infty}^{t} dt' W_{\mathrm{PI}}(t') e^{t'/\tau_r}$$
$$= \tau_r W_{\mathrm{PI}} e^{t/\tau_r} - \tau_r^2 \frac{\partial W_{\mathrm{PI}}}{\partial t} e^{t/\tau_r} + \tau_r^2 \int_{-\infty}^{t} dt' \frac{\partial^2 W_{\mathrm{PI}}(t')}{\partial t'^2} e^{t'/\tau_r}.$$

Assuming slow temporal variations of the photoionization rate on the recombination timescale τ_r, i.e., $\tau_r \dot{W}_{\mathrm{PI}} \ll W_{\mathrm{PI}}$, $\tau_r^2 \ddot{W}_{\mathrm{PI}} \ll \dot{W}_{\mathrm{PI}}$, etc., one gets

$$\int_{-\infty}^{t} dt' W_{\mathrm{PI}}(t') e^{t'/\tau_r} \simeq \tau_r W_{\mathrm{PI}} e^{t/\tau_r}.$$

This approximation is reliable since the photoionization rate (or laser intensity) significantly varies only on the laser pulse duration, which is of the order of 100 ps, i.e., much larger than $\tau_r = 1$ ps. The free electron density then reads $n_{\mathrm{fe}} \simeq n_i + \tau_r W_{\mathrm{PI}}(t)$. We have checked that the latter expression is in a very good agreement with the full numerical simulations.

To determine the solid-to-plasma transition timescale, the time t_c at which the critical plasma density n_c is reached has to be evaluated. It is obtained by solving $n_c = \tau_r W_{\mathrm{PI}}(t_c)$, where n_i has been neglected since $n_c \gg n_i$. The general Keldysh expression for the photoionization rate does not allow us to solve the latter equation due to its complexity. As explained in Appendix A, $W_{\mathrm{PI}} \simeq \sigma_2 I^2$ can be used. Defining the laser intensity as $I(t) = I_0 f(t)$ where $f(t)$ is the temporal envelope, the transition time reads

$$t_c = f^{-1}\left(\frac{1}{I_0}\sqrt{\frac{n_c}{\tau_r \sigma_2}}\right), \tag{B3}$$

where f^{-1} is the inverse function such that $f^{-1} \circ f = I_d$. To this critical time corresponds an intensity $I(t_c)$ which reads $I_c = \sqrt{n_c/\sigma_2\tau_r}$. When this critical intensity is reached, the photoionization rate is large enough to reach the critical plasma density within a few ps. However, the whole history of the interaction, including low intensities, has to be taken into consideration to determine the timescale of the solid-to-plasma transition.

To determine this timescale which corresponds to a temporal interval, a realistic initial condition is needed, especially in the case of a Gaussian profile which leads to a theoretical infinitely long interaction time. We can define an effective starting interaction time t_i when the laser-induced free electron density is of the order of n_i, i.e., $n_i = \tau_r W_{\mathrm{PI}}(t_i)$. Finally, the timescale for the solid-to-plasma transition, Δt_t, is $t_c - t_i$, which reads

$$\Delta t_t = f^{-1}\left(\frac{1}{I_0}\sqrt{\frac{n_c}{\tau_r \sigma_2}}\right) - f^{-1}\left(\frac{1}{I_0}\sqrt{\frac{n_i}{\tau_r \sigma_2}}\right). \tag{B4}$$

In case of a Gaussian temporal shape, it reads

$$\Delta t_t = \tau_{\mathrm{FWHM}}\left[\sqrt{\ln\left(I_0\sqrt{\frac{\tau_r\sigma_2}{n_i}}\right)} - \sqrt{\ln\left(I_0\sqrt{\frac{\tau_r\sigma_2}{n_c}}\right)}\right]. \tag{B5}$$

Following the same reasoning as previously, the influence of the impact ionization can be introduced as long as it is not the main mechanism driving the electron dynamics. The latter can then be described as

$$\frac{\partial n_{\mathrm{fe}}}{\partial t} = W_{\mathrm{PI}}(t) + \beta n_{\mathrm{fe}} - n_{\mathrm{fe}}/\tau_r, \tag{B6}$$

where the term βn_{fe} accounts for the impact ionization, with β depending linearly on the laser intensity and $\tilde{\alpha}$. Still assuming the quasistationary approximation, we obtain

$$n_{\mathrm{fe}} \simeq \left(\frac{1}{\tau_r} - \beta\right)^{-1} W_{\mathrm{PI}}(t). \tag{B7}$$

The assumption that the impact ionization remains a correction ensures that $\tau_r^{-1} - \beta > 0$, Eq. (B7) thus predicting a physically correct behavior. The influence of the impact ionization is equivalent to removing the recombination, i.e., previous considerations still stand by changing τ_r only by the effective characteristic time $\tau_{\mathrm{eff}} = (\tau_r^{-1} - \beta)^{-1}$.

---

[1] S. W. Haan *et al.*, Phys. Plasmas **18**, 051001 (2011).
[2] M. J. Edwards *et al.*, Phys. Plasmas **18**, 051003 (2011).
[3] R. Betti and O. A. Hurricane, Nat. Phys. **12**, 435 (2016).
[4] D. D. Meyerhofer *et al.*, Nucl. Fusion **51**, 053010 (2011).
[5] V. N. Goncharov, T. C. Sangster, R. Betti, T. R. Boehly, M. J. Bonino, T. J. B. Collins, R. S. Craxton, J. A. Delettrez, D. H. Edgell, R. Epstein, R. K. Follet, C. J. Forrest, D. H. Froula, V. Yu. Glebov, D. R. Harding, R. J. Henchen, S. X. Hu, I. V. Igumenshchev, R. Janezic, J. H. Kelly, T. J. Kessler, T. Z. Kosc, S. J. Loucks, J. A. Marozas, F. J. Marshall, A. V. Maximov, R. L. McCrory, P. W. McKenty, D. D. Meyerhofer, D. T. Michel, J. F. Myatt, R. Nora, P. B. Radha, S. P. Regan, W. Seka, W. T. Shmayda, R. W. Short, A. Shvydky, S. Skupsky, C. Stoeckl, B. Yaakobi, J. A. Frenje, M. Gatu-Johnson, R. D. Petrasso, and D. T. Casey, Phys. Plasmas **21**, 056315 (2014).
[6] R. S. Craxton, K. S. Anderson, T. R. Boehly, V. N. Goncharov, D. R. Harding, J. P. Knauer, R. L. McCrory, P. W. McKenty, D. D. Meyerhofer, J. F. Myatt, A. J. Schmitt, J. D. Sethian, R. W. Short, S. Skupsky, W. Theobald, W. L. Kruer, K. Tanaka, R. Betti, T. J. B. Collins, J. A. Delettrez, S. X. Hu, J. A. Marozas,

A. V. Maximov, D. T. Michel, P. B. Radha, S. P. Regan, T. C. Sangster, W. Seka, A. A. Solodov, J. M. Soures, C. Stoeckl, and J. D. Zuegel, Phys. Plasmas **22**, 110501 (2015).

[7] R. Ishizaki and K. Nishihara, Phys. Rev. Lett. **78**, 1920 (1997); Phys. Rev. E **58**, 3744 (1998).

[8] S. X. Hu, P. B. Radha, J. A. Marozas, R. Betti, T. J. B. Collins, R. S. Craxton, J. A. Delettrez, D. H. Edgell, R. Epstein, V. N. Goncharov, I. V. Igumenshchev, F. J. Marshall, R. L. McCrory, D. D. Meyerhofer, S. P. Regan, T. C. Sangster, S. Skupsky, V. A. Smalyuk, Y. Elbaz, and D. Shvarts, Phys. Plasmas **16**, 112706 (2009); S. X. Hu, V. N. Goncharov, P. B. Radha, J. A. Marozas, S. Skupsky, T. R. Boehly, T. C. Sangster, D. D. Meyerhofer, and R. L. McCrory, *ibid.* **17**, 102706 (2010).

[9] P. B. Radha, C. Stoeckl, V. N. Goncharov, J. A. Delettrez, D. H. Edgell, J. A. Frenje, I. V. Igumenshchev, J. P. Knauer, J. A. Marozas, R. L. McCrory, D. D. Meyerhofer, R. D. Petrasso, S. P. Regan, T. C. Sangster, W. Seka, and S. Skupsky, Phys. Plasmas **18**, 012705 (2011).

[10] S. X. Hu, D. T. Michel, A. K. Davis, R. Betti, P. B. Radha, E. M. Campbell, D. H. Froula, and C. Stoeckl, Phys. Plasmas **23**, 102701 (2016).

[11] D. T. Michel, S. X. Hu, A. K. Davis, V. Yu. Glebov, V. N. Goncharov, I. V. Igumenshchev, P. B. Radha, C. Stoeckl, and D. H. Froula, Phys. Rev. E **95**, 051202(R) (2017).

[12] J. L. Peebles, S. X. Hu, W. Theobald, V. N. Goncharov, N. Whiting, P. M. Celliers, S. J. Ali, G. Duchateau, E. M. Campbell, T. R. Boehly, and S. P. Regan, Phys. Rev. E **99**, 063208 (2019).

[13] D. H. Edgell, W. Seka, R. E. Bahr, T. R. Boehly, and M. J. Bonino, Phys. Plasmas **15**, 092704 (2008).

[14] E. G. Gamaly, A. V. Rode, B. Luther-Davies, and V. T. Tikhonchuk, Phys. Plasmas **9**, 949 (2002).

[15] G. M. Petrov and J. Davis, J. Phys. B **41**, 025601 (2008).

[16] B. Rethfeld, Phys. Rev. Lett. **92**, 187401 (2004).

[17] L. V. Keldysh, Zh. Eksp. Teor. Fiz. **47**, 1945 (1964) [Sov. Phys. JETP **20**, 1307 (1965)].

[18] J. R. Penano, P. Sprangle, B. Hafizi, W. Manheimer, and A. Zigler, Phys. Rev. E **72**, 036412 (2005).

[19] B. C. Stuart, M. D. Feit, S. Herman, A. M. Rubenchik, B. W. Shore, and M. D. Perry, Phys. Rev. B **53**, 1749 (1996).

[20] R. R. Gattass and E. Mazur, Nat. Photonics **2**, 219 (2008).

[21] L. Barilleau, G. Duchateau, B. Chimier, G. Geoffroy, and V. Tikhonchuk, J. Phys. D **49**, 485103 (2016).

[22] G. Duchateau, M. D. Feit, and S. G. Demos, J. Appl. Phys. **111**, 093106 (2012).

[23] G. Duchateau, M. D. Feit, and S. G. Demos, J. Appl. Phys. **115**, 103506 (2014).

[24] B. Rethfeld *et al.*, J. Phys. D **50**, 193001 (2017).

[25] N. M. Bulgakova, V. P. Zhukov, Y. P. Meshcheryakov, L. Gemini, J. Brajer, D. Rostohar, and T. Mocek, J. Opt. Soc. Am. B **31**, C8 (2014).

[26] E. G. Gamaly, Phys. Rep. **508**, 91 (2011).

[27] E. G. Gamaly and A. V. Rode, J. Opt. Soc. Am. B **31**, C36 (2014).

[28] A. Kaiser, B. Rethfeld, M. Vicanek, and G. Simon, Phys. Rev. B **61**, 11437 (2000).

[29] L. Spitzer, Jr., *Physics of Fully Ionized Gases* (Interscience Publishers, New York, 1956).

[30] K. Eidmann, J. Meyer-ter-Vehn, T. Schlegel, and S. Hüller, Phys. Rev. E **62**, 1202 (2000).

[31] S. I. Anisimov, B. Kapeliovich, and T. Perel'man, Zh. Eksp. Teor. Fiz. **66**, 776 (1974) [Sov. Phys. JETP **39**, 375 (1974)].

[32] V. N. Goncharov *et al.*, Phys. Rev. Lett. **104**, 165001 (2010).

[33] B. Arad and S. Eliezer, Phys. Rev. A **18**, 2261 (1978).

[34] B. Rethfeld, Phys. Rev. B **73**, 035101 (2006).

[35] G. M. Petrov, J. P. Palastro, and J. Peñano, Phys. Rev. E **95**, 053209 (2017).

[36] A. Colaitis, G. Duchateau, P. Nicolai, and V. Tikhonchuk, Phys. Rev. E **89**, 033101 (2014).